SAND2018-0208J

# Infrared and Raman Spectroscopy of Negative Thermal Expansion Materials: A Comprehensive Density Functional Perturbation Theory and Experimental Study of α-$ZrW_2O_8$

Philippe F. Weck[*,†], Margaret E. Gordon[†], Jeffery A. Greathouse[†], Charles R. Bryan[†], Stephen P. Meserole[†], Mark A. Rodriguez[†], Clay Payne[†] and Eunja Kim[‡]

[†] Sandia National Laboratories, Albuquerque, New Mexico 87185, United States

[‡] Department of Physics and Astronomy, University of Nevada Las Vegas, 4505 Maryland Parkway, Las Vegas, Nevada 89124, United States

**ABSTRACT:** Cubic zirconium tungstate (α-$ZrW_2O_8$), a notorious negative thermal expansion (NTE) material, has been investigated within the framework of density functional perturbation theory (DFPT), combined with experimental characterization to assess and validate computational results. Using combined FT-IR measurements and DFPT calculations, new and extensive assignments were made for the far-infrared (<400 $cm^{-1}$) spectrum of α-$ZrW_2O_8$. A systematic comparison of DFPT-simulated infrared, Raman, and phonon density-of-state spectra with Fourier transform far-/mid-infrared and Raman data collected in this study, as well as with available inelastic neutron scattering measurements, shows the superior accuracy of the PBEsol exchange-correlation functional over standard PBE calculations for studying the spectroscopic properties of materials with anomalous thermal expansion.

## 1. INTRODUCTION

While most materials expand upon heating as a result of anharmonic lattice dynamics,[1] an unusual and fascinating subclass of materials exhibit negative thermal expansion (NTE).[2,3,4,5,6,7,8,9,10] Mechanisms underlying NTE range from structural or magnetic phase transitions to anomalous vibrational modes, such as transverse vibrational modes or rigid unit modes (RUM).[4,6,8,9] NTE has been a subject of active experimental and theoretical research for several decades, with well-documented NTE in materials such as, e.g., Si and Ge, elemental U, $\beta$-quartz, elastomers, some zeolites and ceramics with framework structures.[2,4,5,6,7,9]

Typical NTE materials exhibit anisotropic expansion, *i.e.*, contraction in one or two directions coupled with positive thermal expansion in other directions, over a very limited temperature range.[4,5,6] Owing to this anisotropic expansion, microcracks affecting mechanical strength can develop in such NTE materials, leading to significant hysteresis effect in heating/cooling cycles. Although microcracking can be used advantageously for the development of materials designed to withstand thermal shocks, isotropic NTE materials are usually preferred for most relevant technological applications.[5,6,8] Indeed, isotropic NTE materials can be used as thermal-expansion compensators in composites designed to have overall zero or adjustable thermal expansion.[8] Controlling thermal expansion of materials is of crucial importance, for example, in the production and operation of nanoscale semiconductor devices, high-precision optical systems, or high-performance thermoelectric converters and fuel cells.[5,8,9]

A very few materials, all either cubic or amorphous, feature isotropic NTE over a broad temperature range that includes room temperature. For example, amorphous $SiO_2$, $CuO_2$ and Si possess low-temperature isotropic NTE, and cubic $AV_2O_7$ (A = Zr, Hf) and $AP_2O_7$ (A = Th, U) exhibit isotropic NTE above room temperature.[5] Originally synthesized and characterized in the 1960's,[11,12] zirconium tungstate, $ZrW_2O_8$, with a relatively large and nearly linear NTE of *ca.* $-9\times10^{-6}$ $K^{-1}$ ranging from absolute zero up to its decomposition temperature of ~1050 K, has attracted the most experimental attention among NTE materials only over the last two decades.[13,14,15,16,17,18,19,20,21,22,23,24,25,26,27,28,29] The cubic structure of $ZrW_2O_8$ was solved in the mid 1990's[13,14] and was initially considered to be unstable due to its tedious synthesis. The structure of the low-temperature acentric α-$ZrW_2O_8$ phase (space group $P2_13$) is closely related to $ZrV_2O_7$ (space group $Pa\overline{3}$), with $ZrO_6$ octahedra occupying the unit-cell origin and face centers and two crystallographically distinct $WO_4^{2-}$ tetrahedral units substituting $V_2O_7^{4+}$ groups.[13,14] Upon heating to ~431 K, α-$ZrW_2O_8$ transforms into the centric cubic $\beta$-$ZrW_2O_8$ high-temperature phase (space group $Pa\overline{3}$).[13,15,22]

Contrasting with this wealth of experimental information available on α-$ZrW_2O_8$, very few computational studies have been dedicated to this notorious NTE material, as recently noted by Dove and Fang.[10] Lattice dynamics simulations using classical force fields were conducted by Mittal and Chaplot in 2000,[30] and by Sanson in 2014.[31] To the best of our knowledge, the only first-principles investigations of α-$ZrW_2O_8$ were reported in the past few years by Ramzan et al.,[32] Gava et al.,[33] and Gupta et al.[34] Ramzan and coworkers[32] used density functional theory (DFT), with the Perdew, Burke and Ernzerhof (PBE)[35] exchange-correlation (XC) functional, to study the high-pressure, mechanical and optical properties of α-$ZrW_2O_8$. Gava et al.[33] focused on predicting the mode Grüneisen parameters and NTE behavior of α-$ZrW_2O_8$ using DFT with the hybrid Becke three-parameter Lee-Yang-Parr (B3LYP) XC functional, according to the Debye-Einstein model of the quasiharmonic approximation (QHA). Finally, Gupta and coworkers[34]

reinvestigated in greater detail the specific roles of anharmonic phonons responsible for the large NTE of α-$ZrW_2O_8$ using DFT/PBE. All aforementioned DFT studies used finite displacement methods to determine the interatomic forces and phonon frequencies of α-$ZrW_2O_8$. Very limited assignment exists below 400 $cm^{-1}$ for the far-infrared and Raman spectra of α-$ZrW_2O_8$.

In this work, the infrared (IR), Raman, and phonon density-of-state (PDOS) spectra and vibrational properties of α-$ZrW_2O_8$ have been extensively investigated within the framework of density functional perturbation theory (DFPT), and systematically compared with results from experimental characterization carried out in this study and previous investigations in order to assess and validate DFPT results. DFPT linear response calculations were conducted using the PBE XC functional, utilized in two of the previous DFT studies of α-$ZrW_2O_8$, as well as the revised version of PBE XC for solids (PBEsol).[36] Compared to simple finite-displacement methods typically used with DFT to determine the vibrational properties of many-particle systems, DFPT-based computational approaches can be regarded as considerably more effective, since additional physical properties (e.g., IR and Raman absorbance) can be derived from the total energy with respect to perturbations.[37] The accuracy of DFPT methods was extensively tested in previous lattice dynamics studies.[38,39,40,41,42,43]

Details of our computational and experimental approaches are provided in the next section, followed by a detailed analysis and discussion of our results. A summary of our findings and conclusions is presented in the last section of the manuscript.

## 2. METHODS

**Computational Methods.** First-principles calculations were carried out using DFT, as implemented in the Vienna *ab initio* simulation package (VASP).[44] The XC energy was calculated using the generalized gradient approximation (GGA), with the PBE[35] parameterization and its PBEsol[36] revised version for solids. Both functionals were found in previous studies to correctly describe the geometric parameters and properties of a variety of Zr compounds and oxides.[38,39,40,45,46]

The interaction between valence electrons and ionic cores was described by the projector augmented wave (PAW) method.[47,48] The Zr($4p^6$,$5s^2$,$4d^2$), W($6s^2$,$5d^4$) and O($2s^2$,$2p^4$) electrons were treated explicitly as valence electrons in the Kohn-Sham (KS) equations and the remaining core electrons together with the nuclei were represented by PAW pseudopotentials. The KS equation was solved using the blocked Davidson[49] iterative matrix diagonalization scheme. The plane-wave cutoff energy for the electronic wavefunctions was set to a value of 500 eV, ensuring the total energy of the system to be converged to within 1 meV/atom. A periodic unit-cell approach was used in the total-energy relaxation calculations, with the α-$ZrW_2O_8$ crystal structure (space group $P2_13$, IT No. 198; $Z$ = 4) reported by Evans *et al.*[15] utilized as the initial guess. The Brillouin zone was sampled using the Monkhorst-Pack $k$-point scheme,[50] with a $k$-point mesh of 5×5×5. No symmetry constraints were imposed in unit-cell optimization calculations. Relaxation calculations were first carried out until the Hellmann-Feynman forces acting on atoms were converged within 0.01 eV/Å.

Structures resulting from total-energy minimization with GGA/PBE and GGA/PBEsol were further relaxed with respect to Hellmann-Feynman forces until a convergence tolerance of 0.001 eV/Å was reached. Density functional perturbation theory (DFPT) linear response calculations were then carried out at these levels of theory with VASP to determine the vibrational frequencies and associated intensities. The latter were computed based on the Born effective charges (BEC) tensor, which corresponds to the change in atoms polarizabilities with respect to an external electric field. This DFPT approach was utilized in previous computational studies to successfully predict the properties of various Zr-containing compounds and crystalline materials.[38,39,40,41,45,51,52,53,54]

**Experimental Methods.** All reagents were used as received for the synthesis of α-$ZrW_2O_8$ samples. Accurate metal concentrations in the reagents were determined via thermogravimetric analysis: heating under USP grade air to 900 °C. Following the procedure from Closmann *et al.*,[55] a 1M aqueous solution of tungsten with a volume of 50 mL and a 0.5M aqueous solution of zirconium with a volume of 50 mL were made separately from ammonium metatungstate (Aldrich) and zirconium oxychloride hydrate (Aldrich). Simultaneously, each solution was added dropwise to a stirred flask containing 25 mL deionized (DI) water. After addition, the flask was stirred for an additional 10 hours. Then, 125 mL of 6M HCl was added to the solution and mixed. The solution was placed in a Parr reactor and heated to 200 °C under autogenous pressure for 4 hours. The resulting solution was filtered and rinsed with DI water to obtain $ZrW_2O_7(OH)_2(H_2O)_2$, a cubic hydrated precursor to α-$ZrW_2O_8$ (see Supporting Information). The precursor was then heated to 600 °C for 10 hours, and allowed to cool to ambient temperature.

X-ray Diffraction (XRD) analysis was performed at room temperature using a Bruker D2 Phaser diffractometer. This system was equipped with a sealed-tube X-ray source (Cu $K_\alpha$ radiation, λ = 1.5406 Å) operated at 30 kV and 10 mA. A Ni-filter was employed on the diffracted-beam side of the instrument for suppression of $K_\beta$ radiation. A Lynxeye™ silicon strip detector was employed to collect the diffraction pattern with a scan rate of 15° 2$\theta$ per minute. Samples were analyzed as-received without any additional modification. XRD analysis was performed using the program JADE 9.0 (Materials Data, Inc. Livermore, CA).

Infrared spectra were collected at room temperature using a Thermo Scientific Nicolet 6700 Fourier transform infrared (FT-IR) spectrometer and OMNIC 8.3 software suite, with a Spectra Tech Collector II-DRIFTS (diffuse reflectance) and an aluminum mirror as background and blank; powder was placed in a holder and spectra were collected. Scans were done on the sample at a resolution of 1 $cm^{-1}$, over an absorbance range of 4000.12 to 649.89 $cm^{-1}$, using a KBr beamsplitter and a MCT/A detector. Scans were also carried out with a solid substrate beamsplitter and a DTGS-polyethylene detector using similar resolution in the range 600.23−50.14 $cm^{-1}$, and converted to 4.0 $cm^{-1}$ resolution using the software.

Raman spectra were collected at room temperature using a Horiba T64000 Raman Spectrometer fitted with 1800 grooves/mm gratings and a Symphony CCD detector and controlled with the LabSpec 5 software. A Coherent Verdi V10 green laser (532 nm laser at 50 mW before entering the instrument) was used for excitation. The instrument was calibrated by analyzing a piece of silicon wafer (520.7 $cm^{-1}$). The α-$ZrW_2O_8$ spectrum shown was captured using 11 accumulations of 60 seconds from 50 to 1150 $cm^{-1}$. An Olympus BH2 (BHSM) microscope with a BH2-UMA fitted with a ULWD MS Plan 80 objective (NA= 0.75) was used for sampling the material. Data collection was in the single mode looking between 50 and 1150 $cm^{-1}$.

## 3. RESULTS AND DISCUSSION

**Crystal Structure.** Scanning electron microscope (SEM) characterization of the $ZrW_2O_7(OH)_2(H_2O)_2$ precursor and α-$ZrW_2O_8$ showed similar crystal habits, with elongated thin crystalline plates or filiform pointed needles (see Figure 1 below and Figures S1 and S3 in Supporting Information).

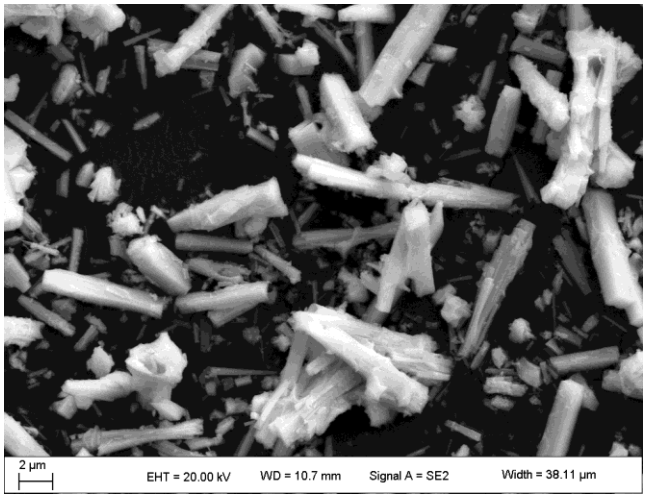


**Figure 1.** Scanning electron microscope (SEM) image of α-$ZrW_2O_8$.

Figure 2 depicts the observed X-ray diffraction pattern of α-$ZrW_2O_8$ (Cu Kα radiation, λ = 1.5406 Å) and simulated patterns from crystal geometries optimized with DFT at the GGA/PBE and GGA/PBEsol levels of theory, with and without relaxation of the experimental crystal lattice. The fully-relaxed structure of cubic α-$ZrW_2O_8$ (space group $P2_13$, IT No. 198; $Z$ = 4) features crystal unit cell parameters of $a$ = 9.241 Å ($V$ = 789.10 Å$^3$) for GGA/PBEsol and $a$ = 9.310 Å ($V$ = 806.87 Å$^3$) for GGA/PBE at $T$ = 0 K. These lattice parameter values in the athermal limit are ~1.0% and ~1.8% larger than the present XRD estimate of 9.1493(2) Å at $T$ = 298 K, due to NTE in the range 0−298 K and to the fact that GGA-type functionals tend to slightly overestimate bond distances. The predicted PBEsol and PBE lattice parameters reproduce within ~0.6% and ~1.4%, respectively, the value of 9.1846(7) Å refined by Evans et al. at $T$ = 0.3 K using a rigid unit model. As shown in Table 1, comparable agreement is obtained with previous DFT and experimental results. Let us note the superior accuracy of the lattice parameter calculated using the PBEsol XC functional over results obtained using the standard PBE functional and the hybrid B3LYP functional (see Figure 2 and Table 1). Relaxation of the unit cell lattice has only a limited impact on the simulated patterns, resulting in a small peak shift towards smaller 2θ values.

A ball-and-stick representation of the α-$ZrW_2O_8$ crystal unit cell is shown in Figure 3(a). As discussed in previous studies, the structure consists of corner-sharing $ZrO_6$ octahedral and two crystallographically distinct $WO_4$ tetrahedral coordination units (with metal centers labeled hereafter as W1 and W2). All atoms are positioned on 4*a* Wyckoff sites (.3. symmetry), with the exception of O1 and O2 atoms on 12*b* Wyckoff sites (1 symmetry). The bond distances calculated in this study with PBEsol and PBE, along with previous PBE and B3LYP results and XRD and neutron diffraction data are summarized in Table 1. The W1 centers possess a tetrahedral local environment with three W1−O1 bonds of 1.823 and 1.832 Å and one shorter W1−O4 bond of 1.729 and 1.732 Å with PBEsol and PBE, respectively [see Figure 3(b)]. Similarly, the local environment of the W2 centers consists of three W2−O2 bonds of 1.798 and 1.810 Å and one shorter W2−O3 bond of 1.752 and 1.755 Å with PBEsol and PBE. Octahedrally-coordinated Zr centers exibit two types of bonds, namely three Zr−O1 bonds of 2.059 and 2.077 Å and three longer Zr−O2 bonds of 2.117 and 2.130 Å predicted with PBEsol and PBE, respectively [see Figure 3(c)].

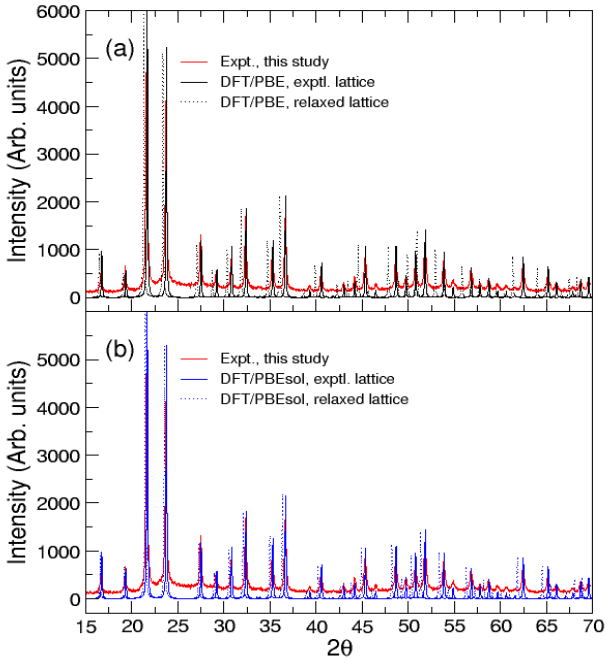


**Figure 2.** Observed X-ray diffraction pattern of α-$ZrW_2O_8$ (Cu Kα radiation, λ = 1.5406 Å) and simulated patterns from crystal geometries optimized with DFT at the (a) GGA/PBE and (b) GGA/PBEsol levels of theory, with and without relaxation of the experimental crystal lattice.

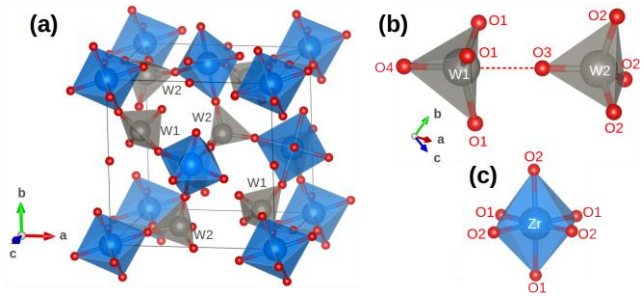


**Figure 3.** (a) Crystal unit cell of α-$ZrW_2O_8$ (space group $P2_13$, IT No. 198; $Z$ = 4), with corner-sharing $ZrO_6$ octahedral (blue) and $WO_4$ tetrahedral (grey) coordination units; (b) Relative arrangement of the two crystallographically distinct $WO_4$ tetrahedra along the threefold symmetry axis (dashed line); (c) $ZrO_6$ coordination octahedron.

As shown in Table 1, the best agreement between DFT results and the low-temperature ($T$ = 0.3 K) bond distances measured by Evans et al. is obtained using the PBEsol functional, followed by PBE and B3LYP functionals.

The PBE bond distances computed in this study are in line with those reported by Gupta et al.[34] at the same level of theory. The bond distances refined from XRD analysis at $T$ = 298 K in this study are overall consistent with previous combined XRD/neutron diffraction structural models by Mary et al.[13] and Evans et al.[15] at $T$ = 293 K

**Table 1. Crystal Structure Properties (in Å) of α-$ZrW_2O_8$ (Space Group $P2_13$, IT No. 198; $Z$ = 4) Calculated with Density Functional Theory and Measured Using X-Ray and Neutron Diffraction.**

| | $T$(K) | $a$ | Zr−O1 | Zr−O2 | W1−O1 | W1−O4 | W2−O2 | W2−O3 |
|---|---|---|---|---|---|---|---|---|
| PBEsol [a] | 0 | 9.241 | 2.059 | 2.117 | 1.823 | 1.729 | 1.798 | 1.752 |
| PBE [a] | 0 | 9.310 | 2.077 | 2.130 | 1.832 | 1.732 | 1.810 | 1.755 |
| PBE [b] | 0 | 9.320 | 2.077 | 2.137 | 1.835 | 1.732 | 1.810 | 1.756 |
| B3LYP [c] | 0 | 9.352 | 2.065 | 2.147 | 1.846 | 1.749 | 1.813 | 1.779 |
| Expt.[d] | 293 | 9.15993(5) | 2.0420 | 2.1085 | 1.7975 | 1.7071 | 1.7819 | 1.7325 |
| Expt.[e] | 293 | 9.1575(2) | 2.0397 | 2.1169 | 1.8011 | 1.7241 | 1.7713 | 1.6940 |
| Expt.[e] | 0.3 | 9.1846(7) | 2.0393 | 2.1131 | 1.8276 | 1.739 | 1.7793 | 1.714 |

[a]This study. [b]Gupta et al., 2013; ref 34. [c]Gava et al., 2012; ref 33. [d]Mary et al., 1996; ref 13 . [e]Evans et al., 1996; ref 15.

.

**Phonon, Infrared, and Raman Spectroscopic Properties.** DFPT was used at the GGA/PBE and GGA/PBEsol levels of theory to calculate the forces exerted on atoms of the equilibrium structure of bulk α-$ZrW_2O_8$ and phonon frequencies were computed at the center of the Brillouin zone (Γ-point) for IR and Raman calculations and along the Γ(0, 0, 0)—X(0, 1/2, 0)—M(1/2, 1/2, 0)—R(1/2, 1/2, 1/2)— **q**=(0, 0, 1/4) — Γ —**q**=(1/4, 1/4, 1/4) —Γ lines in the reciprocal space for the PDOS calculation. Figure 4 shows the resulting phonon density-of-states spectra simulated at $T$ = 0 K, along with generalized PDOS spectrum from inelastic neutron scattering data collected at $T$ = 300 K using time-of-flight (TOF) and filter-analyser (FA) spectroscopy to probe the low and high phonon-energy range, respectively.[18] Overall, good agreement is obtained between DFPT predictions and experiments, with the notable exception of phonon signatures observed in the vicinity of $\omega \cong 600$ cm$^{-1}$, which are not reproduced by calculations. Phonon frequencies calculated with PBEsol appear systematically blueshifted compared to PBE results, with larger differences occurring above $\omega \cong 350$ cm$^{-1}$.

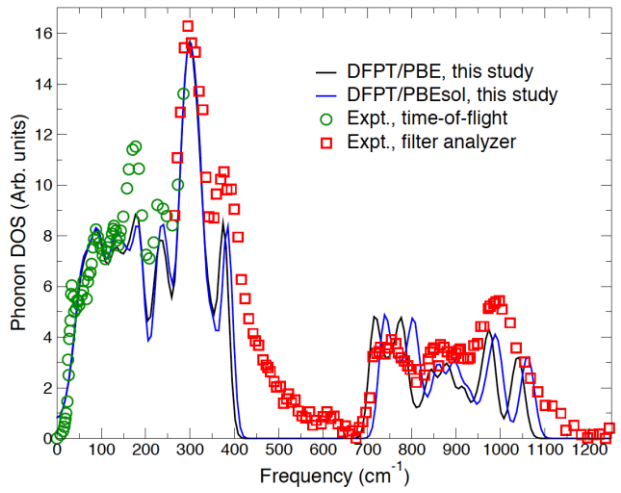


**Figure 4.** Phonon density-of-states (PDOS) spectra of α-$ZrW_2O_8$ simulated at $T$ = 0 K using density functional perturbation theory (DFPT) at the GGA/PBE (black line) and GGA/PBEsol (blue line) levels. The generalized PDOS spectrum from inelastic neutron scattering data collected at $T$ = 300 K using time-of-flight (TOF; green circles) and filter-analyser (FA; red squares) spectroscopy [Ref. (18)] is shown for comparison. A smearing width of σ = 10 cm$^{-1}$ was used to generate PDOS spectra.

With four formula units per unit cell (i.e., $N$ = 44 atoms), α-$ZrW_2O_8$ possesses $3N$ = 132 degrees of freedom, which are distributed among 55 phonons, namely, 54 optical phonons ($\Gamma_{optical}$) and one acoustic phonon ($\Gamma_{acoustic}$). The latter corresponds to triply-degenerate modes of translation at the Γ-point, *i.e.*, one longitudinal acoustic mode and two transverse acoustic modes with zero-frequency, and is associated with the $T$ irreducible representation [irrep; $\Gamma_{acoustic}(3) = T$] of the cubic point group[56] for α-$ZrW_2O_8$ (cf. Table 2). The remaining 129 optical modes can be represented as $\Gamma_{optical}(129) = 11A + 11E + 32T$, where vibrational modes belonging to the $T$, $E$ and $A$ irreps are triply-, doubly- and non-degenerate, respectively. Optical phonons can be further separated into subgroups as follows: $\Gamma_{optical}(129) = \Gamma_{lattice}(9) + \Gamma_{trans}(24) + \Gamma_{libr}(24) + \Gamma_{int}(72)$, where $\Gamma_{lattice}(9) = A + E + 2T$ are lattice modes associated with the motion of Zr atoms, $\Gamma_{trans}(24) = 2A + 2E + 6T$ and $\Gamma_{libr}(24) = 2A + 2E + 6T$ correspond to $WO_4$ modes of translation and libration (*i.e.*, hindered rotation), and $\Gamma_{int}(72) = 6A + 6E + 18T$ are distorted $WO_4$ unit internal modes of vibration. Using a correlation diagram, a direct correspondence can be established between the internal modes of $WO_4$ units in the α-$ZrW_2O_8$ crystal and a free tungstate ion, which features symmetric ($\nu_1$) and antisymmetric ($\nu_3$) stretching modes, as well as symmetric ($\nu_2$) and antisymmetric ($\nu_4$) bending modes.[57,58] The 72 internal modes of $WO_4$ units can be subdivided into the following four categories: $\upsilon_1 \rightarrow 2A + 2T$, $\upsilon_2 \rightarrow 2E + 4T$, $\upsilon_3 \rightarrow 2A + 2E + 6T$, and $\upsilon_4 \rightarrow 2A + 2E + 6T$. A full assignment of the 55 phonons calculated with DFPT at the PBE and PBEsol levels is reported in Table 3. PBEsol (PBE) calculations predict symmetric $\nu_1$ stretching modes in the range 1013−1032 cm$^{-1}$ (993−1012 cm$^{-1}$), antisymmetric $\nu_3$ stretching modes in the range 739−992 cm$^{-1}$ (717−975 cm$^{-1}$), antisymmetric $\nu_4$ and symmetric $\nu_2$ bending modes in the range 277−381 cm$^{-1}$ (276−374 cm$^{-1}$), and a combination of libration, lattice and translation modes below 256 cm$^{-1}$ (253 cm$^{-1}$). Large gaps of 358 cm$^{-1}$ and 343 cm$^{-1}$ computed with PBEsol and PBE, respectively, separate the high-frequency stretching modes from the low-frequency bending modes. These findings are consistent with the 318 cm$^{-1}$ wide gap between 416 and 734 cm$^{-1}$ recently calculated by Gava et al.[33] using DFT with the B3LYP hybrid functional, although spectral signatures were observed in this range in the generalized PDOS spectrum from inelastic neutron scattering data collected at $T$ = 300 K.[18]

**Table 2. Character Table for α-$ZrW_2O_8$ (Space Group $P2_13$, IT No. 198; Cubic Point Group T(23); See ref. 56).**

| Irrep.[a] | Multiplicity | $E$ | $3C_2$ | $4C_3$ | $4(C_3)^2$ | Functions/Rotations |
|---|---|---|---|---|---|---|
| $T$ | 33 | 3 | -1 | 0 | 0 | $(x,y,z)$ $(xy,yz,xz)$ $(R_x,R_y,R_z)$ |
| $E$ | 11 | 2 | 2 | -1 | -1 | $(x^2\text{-}y^2, 3z^2\text{-}r^2)$ |
| $A$ | 11 | 1 | 1 | 1 | 1 | $x^2+y^2+z^2$ |

[a]Vibrational modes belonging to the $T$, $E$ and $A$ irreducible representations (irrep.) are triply-, doubly- and non-degenerate, respectively.

**Table 3. Vibrational Eigenfrequencies for α-$ZrW_2O_8$ (space group $P2_13$, IT No. 198) Calculated from Density Functional Perturbation Theory (DFPT) at the GGA/PBE and GGA/PBEsol Levels. Observed IR- and Raman-Active Bands Are Reported for Comparison.**

| Irrep.[a] | DFPT ($cm^{-1}$) | | IR ($cm^{-1}$) | | Raman ($cm^{-1}$) | | | Mode Description[e] |
|---|---|---|---|---|---|---|---|---|
| | PBE[b] | PBEsol[b] | Expt.[b] | Expt.[c] | Expt.[b] | Expt.[c] | Expt.[d] | |
| *A* | 1012 | 1032 | | | 1030 | $1028_m$ | 1034 | ↑ |
| *T* | 1004 | 1021 | | | 1020 | | 1021 | |
| *A* | 1003 | 1019 | | | | | | $\nu_1(WO_4)$ |
| *T* | 993 | 1013 | | | | | 987 | ↓ |
| *T* | 975 | 992 | 998 | $999_w$ | 969 | $966_w$ | 970 | ↑ |
| *A* | 915 | 919 | | | 931 | $929_m$ | 933 | |
| *T* | 888 | 900 | 908 | $907_m$ | 903 | $901_m$ | 907 | |
| *T* | 850 | 861 | 873 | $871_s$ | | $887_w$ | 890 | |
| *A* | 843 | 855 | | | | $859_w$ | 863 | $\nu_3(WO_4)$ |
| *T* | 771 | 798 | 799 | $800_s$ | | | 807 | |
| *E* | 769 | 796 | | | 792 | $789_s$ | 794 | |
| *T* | 732 | 756 | 760 | $760_m$ | | | 747 | |
| *E* | 721 | 744 | | | 737 | $733_m$ | 737 | |
| *T* | 717 | 739 | 734 | $739_m$ | | | 725 | ↓ |
| *T* | 374 | 381 | 399 | | | | | ↑ |
| *E* | 369 | 377 | | | 383 | $382_w$ | 382 | |
| *T* | 367 | 375 | 393 | | | | | |
| *T* | 347 | 352 | 368 | | | | 350 | |
| *A* | 342 | 346 | | | | | | |
| *T* | 325 | 325 | | | | | | |
| *E* | 320 | 323 | | | 332 | $331_m$ | 331 | |
| *T* | 320 | 321 | 332 | | | | | |
| *T* | 307 | 307 | 321 | | | | | $\nu_4(WO_4)$ |
| *E* | 299 | 300 | | | 309 | $308_w$ | 307 | + |
| *T* | 297 | 299 | | | | | | $\nu_2(WO_4)$ |
| *T* | 291 | 295 | 305 | | | | 298 | |
| *T* | 290 | 292 | | | | | | |
| *A* | 283 | 286 | | | | | | |
| *T* | 283 | 284 | 292 | | | | | |
| *E* | 276 | 277 | | | | 271 | 270 | ↓ |
| *T* | 253 | 256 | 262 | | | | 243 | ↑ |
| *E* | 234 | 238 | | | 235 | $234_w$ | 236 | |
| *T* | 234 | 237 | 240 | | | | | |
| *A* | 233 | 236 | | | | | | |
| *T* | 225 | 228 | 222 | | | | | |
| *A* | 201 | 197 | | | | | 205 | |
| *T* | 187 | 190 | 193 | | 181 | | 181 | |
| *T* | 176 | 177 | 185 | | | | | |
| *T* | 172 | 172 | 174 | | | | | |
| *E* | 169 | 171 | | | | | 170 | |
| *T* | 157 | 152 | 161 | | | | | |
| *E* | 142 | 140 | | | 143 | $144_m$ | 143 | |
| *T* | 128 | 128 | 132 | | | | | |
| *A* | 125 | 123 | | | | | | Libration + Lattice + |
| *T* | 100 | 97 | 97 | | | | | Translation |
| *E* | 94 | 93 | | | 104 | $103_w$ | 113 | |
| *T* | 82 | 91 | 86 | | 77 | $84_w$ | 91 | |
| *A* | 74 | 73 | | | 66 | $65_m$ | 69 | |
| *T* | 68 | 72 | 78 | | | | | |
| *T* | 60 | 64 | 71 | | | | | |
| *T* | 60 | 59 | | | | | | |
| *A* | 51 | 48 | | | | | 50 | |
| *E* | 42 | 37 | | | | $40_m$ | 41 | |
| *T* | 39 | 36 | | | | | | ↓ |
| *T* | 0 | 0 | | | | | | Acoustic |

[a]Vibrational modes belonging to the *T*, *E* and *A* representations are Raman active (quadratic functions), while only *T* modes are IR active (linear functions). [b]This study. [c]Evans et al., 1996; ref 15; Band intensity: $s$ = strong $m$ = medium, $w$ = weak. [d]Ravindran et al., 2001; ref 24. [e] Free tungstate ion vibration modes: symmetric ($\nu_1$) and antisymmetric ($\nu_3$) stretching modes, symmetric ($\nu_2$) and antisymmetric ($\nu_4$) bending modes.

Eigenfrequencies predicted with DFPT have also been systematically compared to IR and Raman bands observed in this study and in previous experiments by Evans et al.[15] and Ravindran et al.[24] (cf. Table 3). As shown in Table 2, all the optical modes belonging to the *T*, *E* and *A* irreps are Raman active (quadratic functions), while only optical modes from the *T* irrep are IR active (linear functions).

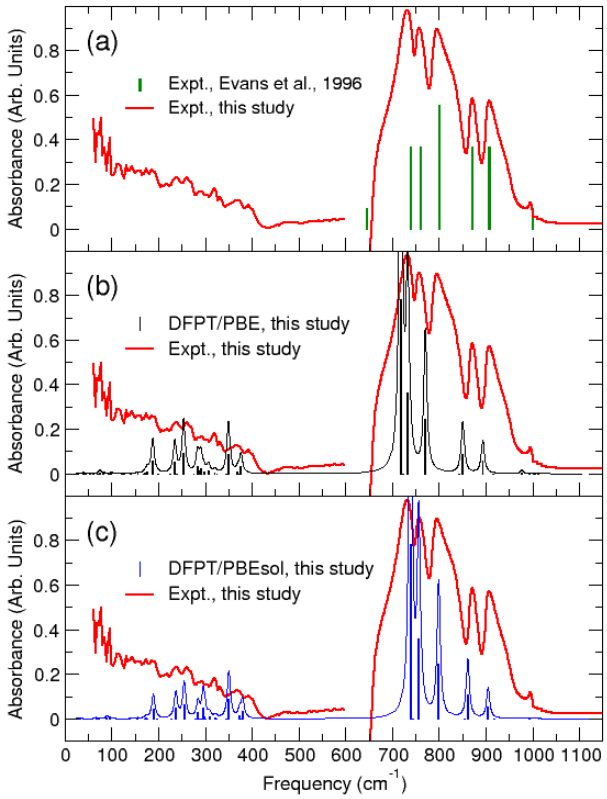


**Figure 5.** (a) Fourier transform infrared (FT-IR) spectrum of α-$ZrW_2O_8$ measured in this study at $T = 298$ K (red line) and observed IR band centers reported by Evans *et al.* [Ref. (15)] (green peaks), along with infrared spectra simulated from density functional perturbation theory (DFPT) at the (b) GGA/PBE (black line/peaks) and (c) GGA/PBEsol (blue line/peaks) levels. Natural line broadening was simulated from DFPT eigenfrequencies using a Lorentzian lineshape function with a full width at half maximum (FWHM) of 4 $cm^{-1}$.

As shown in Table 3 and Figure 5, the FT-IR bands observed by Evans et al.[15] at 999 $cm^{-1}$ (*w*: weak), 907 $cm^{-1}$ (*m*: medium), 871 $cm^{-1}$ (*s*: strong), 800 $cm^{-1}$ (*s*), 760 $cm^{-1}$ (*m*) and 739 $cm^{-1}$ (*m*) are well reproduced by the FT-IR spectrum collected in this study. The IR spectrum simulated using PBEsol is in closer agreement with experiments over this frequency range than that predicted with PBE. The IR-active frequency observed by Evans et al.[15] at 646 $cm^{-1}$ (*w*) along with several weak lines in the range 600-400 $cm^{-1}$ (*w*) (not shown in Figure 5) were not predicted by DFPT calculations, nor observed in the present experiments. This discrepancy is similar to the one mentioned above in the comparison between the generalized PDOS spectrum from inelastic neutron scattering data and PDOS simulated with DFPT. Based on previous FT-IR investigations,[59,60] it can be inferred these additional IR bands observed by Evans et al.[15] originate from the formation of $ZrO_2$ and/or $WO_3$, which are thermodynamically more stable around room temperature than the α-$ZrW_2O_8$ compound.[61]

Using combined FT-IR measurements and DFPT calculations, new and extensive assignments were made for the far-infrared (<400 $cm^{-1}$) spectrum of α-$ZrW_2O_8$. As show in Table 3, seven IR-active bands corresponding to $\nu_4(WO_4)$ and $\nu_2(WO_4)$ were found in the FT-IR spectrum observed between 399 and 292 $cm^{-1}$, in addition to twelve IR bands assigned as libration, lattice and translation modes between 262 and 71 $cm^{-1}$. The lowest-frequency IR-active mode predicted at 36 and 39 $cm^{-1}$ with PBEsol and PBE, respectively, could not be observed in FT-IR experiments.

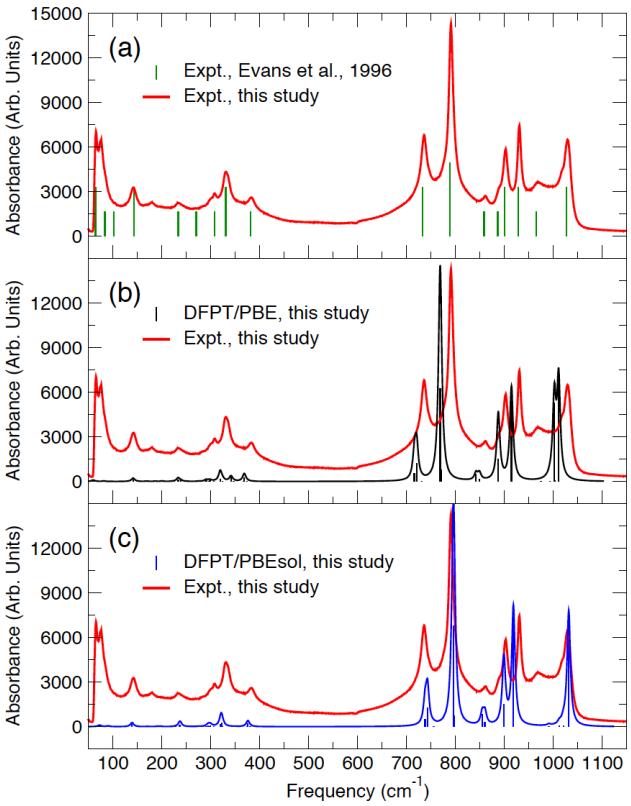


**Figure 6.** Raman spectrum of α-$ZrW_2O_8$ measured in this study at $T = 298$ K (red line) and observed Raman band centers reported by Evans *et al.* [Ref. (15)] (green peaks), along with Raman spectra simulated from density functional perturbation theory (DFPT) at the (b) GGA/PBE (black line/peaks) and (c) GGA/PBEsol (blue line/peaks) levels. Natural line broadening was simulated from DFPT eigenfrequencies using a Lorentzian lineshape function with a full width at half maximum (FWHM) of 4 $cm^{-1}$.

The Raman spectra simulated with DFPT at the PBEsol and PBE levels, along with the Raman-active bands observed at room temperature in this study and by Evans et al.[15] are shown in Figure 6, with the corresponding vibrational eigenfrequencies listed in Table 3, which also includes Raman band centers measured by Ravindran et al.[24] at $T = 20$ K. All three sets of observed Raman bands appear to be consistent overall, although a larger number of Raman-active bands was reported by Ravindran et al.[24] Instead of the fourteen Raman bands expected above 600 $cm^{-1}$ from group theory analysis (cf. Table 3), twenty bands were observed by Ravindran et al.[24] Comparison between their Raman results and PBEsol predictions show that the band observed at 1021 $cm^{-1}$ (1020 $cm^{-1}$ in this study) is actually a combination of two bands predicted at 1021 $cm^{-1}$ (*T* irrep) and 1019 $cm^{-1}$ (*A* irrep). In addition, the bands centers observed by Ravindran et al.[24] at 855, 841, 779, 718, 685, 645 and 628 $cm^{-1}$ do not appear to coincide with any of the α-$ZrW_2O_8$ Raman bands predicted with DFPT or measured in this study or by Evans et al.[15] or by Perottoni and da Jornada.[20] As aforementioned, some of these Raman bands might stem from the presence of stable $ZrO_2$ or $WO_3$ in the sample used by Ravindran et al.[24]. Let us note

that, similar to PDOS and IR DFPT calculations, no Raman active modes are predicted to occur in the ranges 381-739 $cm^{-1}$ and 374-717 $cm^{-1}$ with PBEsol and PBE, respectively.

## 4. CONCLUSION

In summary, DFPT calculations were conducted at the GGA/PBE and GGA/PBEsol levels of theory to systematically investigate the crystal structure, phonon, IR and Raman spectra, and vibrational properties of α-$ZrW_2O_8$. The accuracy of the DFPT methodology was extensively assessed and validated by performing a comprehensive comparison between results from these calculations and experimental data generated in this study and previous investigations.

Relaxed crystal unit-cell parameters of $a$ = 9.24 and 9.31 Å were obtained at $T$ = 0 K with PBEsol and PBE, respectively, *i.e.*, ~0.6% and ~1.4% larger than the value of 9.1823(4) Å measured by Evans et al. at $T$ = 0.3 K, and ~1.0% and ~1.8% larger than the present XRD estimate of 9.1493(2) Å at room temperature. The accuracy of the PBEsol XC functional in reproducing experimental crystallographic parameters is superior compared to the standard PBE and hybrid B3LYP functionals

In addition, good agreement was obtained between the phonon density of states spectra simulated with DFPT in the athermal limit and the generalized PDOS spectrum from inelastic neutron scattering data collected at $T$ = 300 K using time-of-flight and filter-analyser spectroscopy to probe the low and high phonon-energy range. The only notable exception was for phonon signatures observed in the vicinity of $\omega \cong 600$ $cm^{-1}$, which are not reproduced by DFPT calculations. Phonon frequencies calculated with PBEsol appear systematically blueshifted compared to PBE results, with larger differences occurring above $\omega \cong 350$ $cm^{-1}$.

A full assignment of the 55 phonons of α-$ZrW_2O_8$ was reported based on PBE/PBEsol DFPT calculations and eigenfrequencies predicted with DFPT were systematically compared to IR and Raman bands observed in this study and in previous experiments by Evans et al. and Ravindran et al. From the direct correspondence between the internal modes of $WO_4$ units in the α-$ZrW_2O_8$ crystal and a free tungstate ion, PBEsol (PBE) calculations predicted symmetric $\nu_1$ stretching modes in the range 1013−1032 $cm^{-1}$ (993−1012 $cm^{-1}$), antisymmetric $\nu_3$ stretching modes in the range 739−992 $cm^{-1}$ (717−975 $cm^{-1}$), antisymmetric $\nu_4$ and symmetric $\nu_2$ bending modes in the range 277−381 $cm^{-1}$ (276−374 $cm^{-1}$), and a combination of libration, lattice and translation modes below 256 $cm^{-1}$ (253 $cm^{-1}$). Large gaps of 358 $cm^{-1}$ and 343 $cm^{-1}$ computed with PBEsol and PBE, respectively, separate the high-frequency stretching modes from the low-frequency bending modes, although spectral signatures were previously observed in this range in the generalized PDOS spectrum from inelastic neutron scattering.

The present results and finding demonstrate the accuracy of the DFPT/PBEsol approach for studying the spectroscopic and vibrational properties of stoichiometric materials with anomalous thermal expansion. Further DFPT investigations will focus on the role of defects and impurities in NTE materials, since a full understanding of the structure-property relationship is currently absent for this class of systems.

## ASSOCIATED CONTENT

## AUTHOR INFORMATION

### Corresponding Author

*E-mail pfweck@sandia.gov; Ph 505-844-8144 (P.F.W.).

### Notes

The authors declare no competing financial interests.

## ACKNOWLEDGMENT

Sandia National Laboratories is a multi-mission laboratory managed and operated by National Technology and Engineering Solutions of Sandia, LLC., a wholly owned subsidiary of Honeywell International, Inc., for the U.S. Department of Energy's National Nuclear Security Administration under Contract DE-NA0003525. This work was supported by Laboratory Directed Research and Development (LDRD) funding from Sandia National Laboratories.

### Supporting Information

Experimental details of the precipitation of the cubic hydrated precursor $ZrW_2O_7(OH)_2(H_2O)_2$ and conversion to the final α-$ZrW_2O_8$ phase and SEM and XRD characterization of these compounds.

## REFERENCES

[1] Kittel, C. *Introduction to Solid State Physics*, 7th ed., Wiley, New York, 1996.

[2] Chu, C. N.; Saka, N.; Suh, N. P. Negative Thermal Expansion Ceramics: A Review. *Mater. Sci. Eng*. **1987**, *95*, 303–308.

[3] Roy, R.; Agrawal, D. K.; McKinstry, H. A. Very Low Thermal Expansion Coefficient Materials. *Ann. Rev. Matter. Sci*. **1989**, *19*, 59–81.

[4] White, G. K. Solids: Thermal Expansion and Contraction. *Contemp. Phys*. **1993**, *34*, 193.

[5] Sleight, A. W. Isotropic Negative Thermal Expansion. *Ann. Rev. Matter. Sci.* **1998**, *28*, 29–43.

[6] Evans, J. S. O. Negative Thermal Expansion Materials. *J. Chem. Soc. Dalton Trans.* **1999**, 3317–3326.

[7] Barrera, G. D.; Bruno, J. A. O.; Barron, T. H. K.; Allan, N. L. Negative Thermal Expansion. *J. Phys.: Condens. Matter* **2005**, *17*, R217.

[8] Takenaka, K. Negative Thermal Expansion Materials: Technological Key for Control of Thermal Expansion. *Sci. Technol. Adv. Mater*. **2012**, *13*, 013001.

[9] Lind, C. Two Decades of Negative Thermal Expansion Research: Where Do We Stand? *Materials* **2012**, *5*, 1125– 1154.

[10] Dove, M. T.; Fang, H. Negative Thermal Expansion and Associated Anomalous Physical Properties: Review of the Lattice Dynamics Theoretical Foundation. *Rep. Prog. Phys.* **2016**, *79*, 066503.

[11] Graham, J.; Wadsley, A. D., Weymouth, J. H.; Williams, L. S. A new ternary oxide, $ZrW_2O_8$. *J. Am. Ceram. Soc*. **1959**, *42*, 570.

[12] Martinek, C.; Hummel, F.A. Linear Thermal Expansion of Three Tungstates. *J. Am. Ceram. Soc.* **1968**, *51*, 227–228.

[13] Auray, M.; Quarton, M.; Leblanc, M. Zirconium Tungstate. *Acta Crystallogr. C* **1995**, *51*, 2210-2213.

[14] Mary, T. A.; Evans, J. S. O.; Sleight, A. W.; Vogt, T. Negative Thermal Expansion from 0.3 to 1050 Kelvin in $ZrW_2O_8$. *Science* **1996**, *272*, 90-92.

[15] Evans, J. S. O.; Mary, T. A.; Vogt, T.; Subramanian, M. A.; Sleight, A. W. Negative Thermal Expansion in $ZrW_2O_8$ and $HfW_2O_8$. *Chem. Mater*. **1996**, *8*, 2809-2823.

[16] Evans, J. S. O.; Hu, Z.; Jorgensen, J. D.; Argyriou, D. N.; Short, S.; Sleight, A. W. Compressibility, Phase Transitions, and Oxygen Migration in Zirconium Tungstate, $ZrW_2O_8$. *Science* **1997**, *275*, 61-65.

[17] Evans, J. S. O.; David, W. I. F., Sleight, A. W. Structural Investigation of the Negative-Thermal-Expansion Material $ZrW_2O_8$. *Acta Crystallogr.B* **1999**, *55*, 333-340.
[18] Ernst, G.; Broholm, C.; Kowach, G. R.; Ramirez, A. P. Phonon density of states and negative thermal expansion in $ZrW_2O_8$. *Nature* **1998**, *396*, 147-149.
[19] David, W. I. F.; Evans, J. S. O.; Sleight, A. W. Direct Evidence for a Low-Frequency Phonon Mode Mechanism in the Negative Thermal Expansion Compound $ZrW_2O_8$. *Europhys. Lett.* **1999**, *46*, 661-666.
[20] Perottoni, C.A.; da Jornada, J.A.H. Pressure-Induced Amorphization and Negative Thermal Expansion in $ZrW_2O_8$. *Science* **1998**, *280*, 886-889.
[21] Ramirez, A. P.; Kowach, G. Large Low Temperature Specific Heat in the Negative Thermal Expansion Compound $ZrW_2O_8$. *Phys. Rev. Lett.* **1998**, *80*, 4903-4906.
[22] Yamamura, Y.; Nakajima, N.; Tsuji, T. Heat Capacity Anomaly Due to the α to β Structural Phase Transition in $ZrW_2O_8$. *Solid. State Commun*. **2000**, *114*, 453–455.
[23] Ravindran, T. R.; Arora, A. K.; Mary, T. A. High Pressure Behavior of $ZrW_2O_8$: Grüneisen Parameter and Thermal Properties. *Phys. Rev. Lett*. **2000**, *84*, 3879.
[24] Ravindran, T. R.; Arora, A. K.; Mary, T. A. High-Pressure Raman Spectroscopic Study of Zirconium Tungstate. *J. Phys: Condens. Matter* **2001**, *13*, 11573-11588.
[25] Drymiotis, F. R.; Ledbetter, H.; Betts, J. B.; Kimura, T.; Lashley, J. C., Migliori, A.; Ramirez, A.; Kowach, G.; Van Dujin, J. Monocrystal Elastic Constants of the Negative-Thermal-Expansion Compound Zirconium Tungstate ($ZrW_2O_8$). *Phys. Rev. Lett.* **2004**, *93*, 025502.
[26] Jason N. Hancock, Chandra Turpen, and Zack Schlesinger, Glen R. Kowach, Arthur P. Ramirez. *Phys. Rev. Lett*. **2004**, *93*, 225501.
[27] Keen, D. A.; Goodwin, A. L.; Tucker, M. G.; Dove, M. T.; Evans, J. S. O.; Crichton, W. A.; Brunelli, M. Structural Description of Pressure-Induced Amorphization in $ZrW_2O_8$. *Phys. Rev. Lett*. **2007**, *98*, 225501.
[28] Bridges, F.; Keiber, T.; Juhas, P.; Billinge, S. J. L.; Sutton, L.; Wilde, J.; Kowach, G. R. Local Vibrations and Negative Thermal Expansion in $ZrW_2O_8$. *Phys. Rev. Lett*. **2014**, *112*, 045505.
[29] Stevens, R.; Linford, J.; Woodfield, B. F.; Boerio-Goates, J.; Lind, C.; Wilkinson, A. P.; Kowach, G. Heat Capacities, Third-Law Entropies and Thermodynamic Functions of the Negative Thermal Expansion Materials, Cubic a-$ZrW_2O_8$ and Cubic $ZrMo_2O_8$, From $T$ = (0 to 400 K). *J. Chem. Thermo*. **2003**, *35*, 919–937.
[30] Mittal, R.; Chaplot, S. L. Phonon Density of States and Thermodynamic Properties in Cubic and Orthorhombic Phases of $ZrW_2O_8$. *Solid State Communications* **2000**, *115*, 319–322.
[31] Sanson, A. Toward an Understanding of the Local Origin of Negative Thermal Expansion in $ZrW_2O_8$: Limits and Inconsistencies of the Tent and Rigid Unit Mode Models. *Chem. Mater*. **2014**, *26*, 3716-3720.
[32] Ramzan, M.; Luo, W.; Ahuja, R. High Pressure, Mechanical, and Optical Properties of $ZrW_2O_8$. *J. Appl. Phys*. **2011**, *109*, 033510.
[33] Gava, V.; Martinotto, A. L.; Perottoni, C. A. First-Principles Mode Grüneisen Parameters and Negative Thermal Expansion in α-$ZrW_2O_8$. *Phys. Rev. Lett*. **2012**, *109*, 195503.
[34] Gupta, M. K.; Mittal, R.; Chaplot, S. L Negative Thermal Expansion in Cubic $ZrW_2O_8$: Role of Phonons in the Entire Brillouin Zone from Ab Initio Calculations. *Phys. Rev. B* **2013**, *88*, 014303.
[35] Perdew, J. P.; Burke, K.; Ernzerhof, M. Generalized Gradient Approximation Made Simple. *Phys. Rev. Lett*. **1996**, *77*, 3865-3868.
[36] Perdew, J. P.; Ruzsinszky, A.; Csonka, G. I.; Vydrov, O. A.; Scuseria, G. E.; Constantin, L. A.; Zhou, X.; Burke, K. Restoring the Density-Gradient Expansion for Exchange in Solids and Surfaces. *Phys. Rev. Lett.* **2008**, *100*, 136406-.
[37] Gonze, X.; Lee, C. Dynamical matrices, Born effective charges, dielectric permittivity tensors, and interatomic force constants from density-functional perturbation theory. *Phys. Rev. B* **1997**, *55*, 10355.
[38] Weck, P. F.; Kim, E. Assessing Hubbard-Corrected AM05+U and PBEsol+U Density Functionals for Strongly Correlated Oxides $CeO_2$ and $Ce_2O_3$. *Chem. Phys. Phys. Chem*. **2016**, *18*, 26816-26826.
[39] Weck, P. F.; Kim, E. Uncloaking the Thermodynamics of the Studtite to Metastudtite Shear-Induced Transformation. *J. Phys. Chem. C* **2016**, *120*, 16553-16560.
[40] Weck, P. F.; Kim, E.; Tikare, V.; Mitchell, J. A. Mechanical Properties of Zirconium Alloys and Zirconium Hydrides Predicted from Density Functional Perturbation Theory. *Dalton Trans*. **2015**, *44*, 18769-18779.
[41] Johnson, T. J.; Sweet, L. E.; Meier, D. E.; Mausolf, E. J.; Kim, E.; Weck, P. F.; Buck, E. C.; McNamara, B. K. Time-Resolved Infrared Reflectance Studies of the Dehydration-Induced Transformation of Uranyl Nitrate Hexahydrate to the Trihydrate Form. *J. Phys. Chem. A* **2015**, *119*, 9996-10006.
[42] Weck, P. F.; Kim E. Layered uranium(VI) hydroxides: structural and thermodynamic properties of dehydrated schoepite α-$UO_2(OH)_2$. *Dalton Trans.* **2014**, *43*, 17191.
[43] Weck, P. F.; Kim E. Solar Energy Storage in Phase Change Materials: First-Principles Thermodynamic Modeling of Magnesium Chloride Hydrates. *J. Phys. Chem. C* **2014**, *118*, 4618.
[44] Kresse, G.; Furthmüller, J. Efficient Iterative Schemes for Ab Initio Total-Energy Calculations Using a Plane-Wave Basis Set. *Phys. Rev.* B **1996**, *54*, 11169-11186.
[45] Weck, P. F.; Juan, P.-A.; Dingreville, R.; Kim, E. Density Functional Analysis of Fluorite-Structured $(Ce,Zr)O_2/CeO_2$ Interfaces. *J. Phys. Chem. C* **2017**, *121*, 14678.
[46] Colmenero, F.; Bonales, L. J.; Cobos, J.; Timon, V. Density Functional Theory Study of the Thermodynamic and Raman Vibrational Properties of gamma-$UO_3$ Polymorph. *J. Phys. Chem. C* **2017**, *121*, 14507–14516.
[47] Blöchl, P. E. Projector Augmented-Wave Method. *Phys. Rev.* B **1994**, *50*, 17953-17979.
[48] Kresse, G.; Joubert, D. From Ultrasoft Pseudopotentials to the Projector Augmented-Wave Method. *Phys. Rev.* B **1999**, *59*, 1758-1775.
[49] Davidson, E. R. *Methods in Computational Molecular Physics*, G. H. F. Diercksen and S. Wilson, Eds., Vol. 113, NATO Advanced Study Institute, Series C, Plenum, New York, 1983, p. 95.
[50] Monkhorst, H. J.; Pack, J. D. Special Points for Brillouin-Zone Integrations. *Phys. Rev.* B **1976**, *13*, 5188-5192.
[51] Colmenero, F.; Bonales, L.J.; Cobos, J.; Timon, V. Thermodynamic and Mechanical Properties of the Rutherfordine Mineral Based on Density Functional Theory. *J. Phys. Chem. C* **2017**, *121*, 5994-6001.
[52] Weck, P. F.; Kim, E.; Buck, E. C. On the Mechanical Stability of Uranyl Peroxide Hydrates: Implications for Nuclear Fuel Degradation. *RSC Adv*. **2015**, *5*, 79090-79097.
[53] Weck, P. F.; Kim, E.; Jove-Colon, C. F. Relationship Between Crystal Structure and Thermo-Mechanical Properties of Kaolinite Clay: Beyond Standard Density Functional Theory. *Dalton Trans*. **2015**, *44*, 12550-12560.
[54] Weck, P. F.; Kim, E. Thermodynamics of Technetium: Reconciling Theory and Experiment Using Density Functional Perturbation Analysis. *Dalton Trans*. **2015**, *44*, 12735-12742.
[55] Closmann, C.; Sleight, A. W.; Haygarth, J. C. Low-Temperature Synthesis of $ZrW_2O_8$ and Mo-Substituted $ZrW_2O_8$. *J. Sol. State Chem*. **1998**, *139*, 424-426.
[56] Dresselhaus, M. S.; Dresselhaus, G.; Jorio, A. *Group Theory: Application to the Physics of Condensed Matter*, Springer-Verlag, Berlin, 2008, p. 479.
[57] Turel, G. *Infrared and Raman Spectra of Crystals*, Academic Press, New York, 1972.
[58] Herzberg, G. *Molecular Spectra and Molecular Structure. Vol.2: Infrared and Raman Spectra of Polyatomic Molecules*, Van Nostrand-Reinhold, New York, 1962.
[59] Phillippi, C. M.; Mazdiyasni, K. S. Infrared and Raman Spectra of Zirconia Polymorphs. *J. Am. Ceram. Soc*. **1971**, *54*, 254-258.
[60] Gabrusenoks, J.; Veispals, A.; von Czarnowski, A.; Meiwes-Broer, K.-H. Infrared and Raman Spectroscopy of $WO_3$ and $CdWO_4$. Electrochimica Acta **2001**, *46*, 2229-2231.
[61] Chang, L.L.Y.; Scroger, M. G.; Phillips, B. Condensed Phase Relations in Systems $ZrO_2$-$WO_2$-$WO_3$ and $HfO_2$-$WO_2$-$WO_3$. *J. Am. Ceram. Soc.* **1967**, *50*, 211.